Circulation Control as a Roll Effector for Unmanned Combat Aerial Vehicles

G. Hoholis * and R. Steijl † and K. Badcock ‡

University of Liverpool, Liverpool, L69 3GH, United Kingdom

This paper reports on a numerical investigation of the use of trailing edge circulation control as a roll effector on a generic unmanned combat aerial vehicle (UCAV), the DLR-F19 Stability and Control CONfiguration (SACCON). The coanda effect induced by fluidic injections at the trailing edge of a wing is used to increase circulation and generate lift. RANS predictions have been validated against wind tunnel experiments conducted at the Georgia Institute of Technology and NASA's basic aerodynamic research tunnel on an aerofoil employing trailing edge circulation control. Two turbulence models were used, the Wilcox k-ω model and Menter's Shear Stress Transport, showing that the Wilcox k-ω model provides the best comparisons with the experimental data. Baseline data for the SACCON with conventional control surfaces from wind tunnel experiments done at the DNW-NWB wind tunnel are used to ensure the correct flow features are being modelled for the flows encountered by this type of UCAV and to provide a comparison for the performance of the circulation control devices. Modifications have been made to the DLR-F19, replacing the conventional control surfaces with trailing edge circulation control of the same spanwise extent. This includes two configurations, one with a single slot and one with three slots of equal width along the wing. The circulation control performs well at low angles of attack producing a similar roll moment to the conventional control surfaces. Due to the flow separation at the high angles of attack the circulation control is unable to generate a rolling moment. Finally, the flow topology is examined to understand the causes of the decrease in the performance.

Nomenclature

*PhD student, CFD Laboratory, School of Engineering, University of Liverpool, Walker Building, Liverpool L69 3GH.
†Lecturer, CFD Laboratory, School of Engineering, University of Liverpool, Walker Building, Liverpool L69 3GH.
‡Professor, CFD Laboratory, School of Engineering, University of Liverpool, Walker Building, Liverpool L69 3GH.

AVT	Applied Vehicle Technology	BART	Basic Aerodynamic Research Tunnel
CC	Circulation Control	CFD	Computational Fluid Dynamics
C_d	Section drag coefficient	C_D	Drag coefficient
C_l	Section lift coefficient	C_l	Rolling moment coefficient
C_L	Lift coefficient	C_m	Pitching moment coefficient
C_p	Pressure coefficient	C_μ	Blowing coefficient
FLAVIIR	Flapless Air Vehicle Integrated Industrial Research	GACC	General Aviation Circulation Control
GTRI	Georgia Tech Research Institute	IB	Inboard
LDV	Laser Doppler Velocimetry	LES	Large Eddy Simulation
LIB	Left InBoard	LOB	Left OutBoard
$\dot{m}_j$	Jet massflow	MB	Midboard
NASA	National Aeronautics and Space Administration	NATO	North Atlantic Treaty Organisation
NCCR	Navy Circulation Control Rotor Organisation	NPR	Nozzle Pressure Ratio, $\frac{p_{t,j}}{p_\infty}$
OB	Outboard	$p_{t,j}$	Total pressure in plenum chamber
p_∞	Freestream pressure	PMB	Parallel Multi Block
PIV	Particle Image Velocimetry	q_∞	Dynamic pressure
RANS	Reynolds-Averaged Navier Stokes	RET	Ratio of turbulent eddy viscosity to molecular viscosity
RIB	Right InBoard	ROB	Right OutBoard
R	Gas constant	SST	Shear Stress Transport
STOL	Short Take-Off and Landing	SACCON	Stability and Control CONfiguration
S	Wing area	$T_{t,j}$	Total temperature in plenum chamber
u_j	Jet velocity at the slot	U(C)AV	Unmanned (Combat) Aerial Vehicle
γ	Specific heat capacity ratio		

I. Introduction

Circulation control (CC) is the use of fluidic injections and the coanda effect at the trailing edge to modify the lift generated by a wing. Some of the benefits that are often mentioned relative to mechanical control surfaces are a reduction in weight and maintainance due to the lack of mechanically moving parts. Early research into CC was for use as a high-lift device on fixed wing short take-off and landing aircraft.[1,2] The West Virginia University CC demonstrator[3] and the US Navy A-6A[4] were built and flown to show the effectiveness of this concept. Research during this time focused on determining the relationship between the lift generated and the coanda radius or the secondary injection's momentum.[5] The GACC wing designed by NASA introduced the use of two slots, one on the upperside of the coanda surface and one on the lower.[6,7] The purpose of this was that during cruise conditions both slots could be used at the same time to reduce the drag penalty of the bluff trailing edge. Also using only the lower slot allows for negative lift to be generated. Recent research at the University of Manchester and Cranfield University has investigated the use of CC on flapless aircraft to replace conventional control surfaces as a means of aircraft control.[8–10] These papers are a result of the FLAVIIR research programme, which built a UAV to demonstrate new technologies such as circulation control and fluidic thrust vectoring. The circulation control is used to provide roll and pitch control in this case. Work is done in[10] to show that CC effects the control moments of an aerofoil in a similar way to flaps, and modifications to a datasheet method for flaps were made to determine sizing requirements and performance of CC devices.

Some of the early work done in the simulation of these devices[11] used potential flow analysis, with a modification to include effects of viscosity, to optimise the shape of the trailing edge for lift augmentation. Later research started using the RANS equations for 2D simulations of a CC aerofoil specifically designed for validation.[12] Overall good agreement with experimental results was obtained, however certain characteristics that are turbulence dependent such as the separation point were found to be inadequately predicted. At a more recent CC workshop in 2004[13] CFD practitioners were asked to simulate a specific benchmark geometry, the NCCR 1510-7067N for which extensive experimental data is available.[14] This was done to establish a database of simulations for various CFD codes employing different turbulence models and gridding techniques to determine the requirements for the accurate prediction of coanda jets. Several turbulence models were tested without a clear conclusion as to the necessary requirements of simulating the flow physics accurately.[15,16] Following this a new CFD validation test case was designed by NASA and the Georgia Institute of Technology.[17] Work done on this aerofoil includes a comparison between RANS and LES approaches[18] and 3D simulations including wind tunnel walls[19] to quantify the effects of the walls. Some of the RANS turbulence models were capable of predicting the same jet separation point relative to the LES results, however, there were still differences in the lift coefficient and further investigation is needed to understand the causes.

Delta wing planforms exhibit non-linear vortical flow at the higher angles of attack making it difficult to accurately predict their stability and control characteristics. A NATO task group, the AVT-161, was established to try and determine the current ability of CFD methods to predict the stability of this type of aircraft. An overview of the group's aims and methods are discussed in.[20] An integrated approach using experimental and computational methods was used to try and understand the complex flowfield that develops for such configurations. Two configurations were chosen for this purpose, the SACCON (Stability and Control CONfiguration) and the X-31. Experimental work has been done on the SACCON in order to obtain static and dynamic aerodynamic loads[21,22] and PIV data[23,24] for CFD validation purposes. In conjunction with this, CFD simulations were performed[25,26] to determine the capability of prediction codes.

The focus of this work is the investigation of CC as a manoeuvre effector to replace conventional control surfaces on UAVs using CFD. A brief description of the CFD code that is used throughout this paper is given in section 2. This is followed by two validation cases to demonstrate that the CFD code can reliably predict the loads and moments for such applications. The first case is a CC aerofoil designed by NASA and GTRI that was mentioned earlier, discussed in section 3. The second is the SACCON UAV which is discussed in section 4. Modifications are made to the SACCON to replace the flaps with CC in section 5. The effect of the CC on the flowfield and its effectiveness over an angle of attack range is then investigated to determine if it could potentially be used as a control method. Further modifications are made to the CC device to include mutltiple slots along the span. The usual method for controlling the circulation around the wing is varying the NPR, this is the pressure ratio between the air in the plenum chamber and the freestream flow. Multiple slots allow for a different method of controlling the amount of roll moment generated, by using a different number of slots along the span.

II. CFD Formulation

The CFD code used throughout this paper is the parallel multi-block solver (PMB).[27] PMB uses a cell-centered finite volume formulation on block-structured grids to discretise the RANS equations. Osher's approximate Riemann solver is used for the convective fluxes and a two-equation turbulence model, usually the Wilcox k-ω or Menter's SST. Variable extrapolation is used to get second-order accuracy with the Van Albada limiter to prevent oscillations around shockwaves. The mean and turbulent equations are solved decoupled in an implicit manner, with approximate Jacobian matrices based on the first order sparsity pattern, and a Krylov subspace iterative solver. For the boundary conditions halo cells, extrapolated from the block interior, are used. At the farfield an undisturbed freestream boundary condition is imposed. At the beginning of the plenum chamber a reservoir boundary condition is used. The velocities and turbulence variables for the halo cells are extrapolated from the interior. The isentropic flow equations are then used to calculate the density and pressure.

III. Coanda Jet CFD Validation

The CC-E0020EJ circulation control aerofoil has been designed at the Georgia Institute of Technology (GTRI) for CFD validation purposes.[17,28] A simple geometry with a large trailing edge radius was chosen to make it easier to obtain accurate experimental data on the coanda surface. The aerofoil has a chord length of 0.218m, with an elliptical forebody, straight afterbody and thickness to chord ratio of 20%. A first series of tests was done at the GTRI model test facility. The emphasis was put on the performance of the aerofoil and the effect of the slot height. The trailing edge radius is 9.5% of the chord length and the slot height is 0.508mm and the slot lip is 0.254mm. See reference[17] for more details on the construction of the geometry and the wind tunnel experiments. The aerofoil has upper and lower CC slots, with the lower one sealed off for the wind tunnel experiments. A second series of tests was done at NASA's BART installation. These focused on flow characteristics for CFD validation. Surface pressure coefficients, aerodynamic loads and the massflow through the slot were recorded for this set of results.

A few issues were observed from the first two sets of wind tunnel experiments and the CFD solutions that were done alongside them. This led to the internal geometry of the aerofoil being modified to eliminate recirculation zones within the secondary plenum chamber to simplify the internal flow in an attempt to reduce possible sources of discrepancy between experimental results and CFD results.[28] Also measurements of the outer geometry and the end of the second plenum were made, which consist of about 1450 points that have not been smoothed. Three different test cases were run, with low, mid and high levels of blowing which correspond to blowing coefficients of approximately 0.047, 0.115 and 0.150 respectively, where

$$C_\mu = \frac{\dot{m}_j u_j}{q_\infty S} \tag{1}$$

with

$$u_j = \sqrt{\frac{2}{\gamma - 1}\gamma R T_{t,j}\left(1 - \left(\frac{p_j}{p_{t,j}}\right)^{\frac{\gamma-1}{\gamma}}\right)} \tag{2}$$

and the massflow rate is recorded during the experiment.

Table 1 summarises the available data for the aerofoil with the simplified internal geometry.

	Chordwise C_p	Spanwise C_p	LDV Upper/lower surface velocity profiles
$C_\mu \approx 0.047$	Yes	Yes	Yes
$C_\mu \approx 0.115$	Yes	Yes	Yes
$C_\mu \approx 0.150$	Yes	Yes	No

Table 1: Experimental results available from.[28]

The second data set is used for comparison as it is the most recent data set and the measured geometry as opposed to the ideal geometry is known. Also, the simplified internal geometry makes it possible to generate a higher quality mesh within the secondary plenum.

A. Grids and Computational Setup

A group of multi-block grids was generated using the ANSYS ICEM software package. A short description of the grids follows with the coarser grids being constructed by reducing the cells along each block edge by various factors, see table 2.

Grid	Characteristic Number of Cells Along Each Edge	Total Cells
Fine	100	287,200
Medium	80	183,808
Coarse	60	103,392
Extra Coarse	50	71,800

Table 2: Grids used for the refinement study to ensure grid-independent solutions.

A C-grid topology is used at both the leading and trailing edges. The first cell spacing normal to the aerofoil surface is 1×10^{-5} of the chord. The farfield is 10 chords away in all directions. See fig. 1 for the overall topology and close-ups of some of the key locations.

The Mach and Reynolds numbers in the wind tunnel varied slightly for each run, see table 3 for details, which were replicated in the CFD simulation. The turbulence models used were the k-ω and Menter's SST. All the simulations were run as steady-state calculations, the reason for this is discussed in section 3.2. This work is being done as preparation for developing reduced order modelling methods. Therefore, we are interested in the loads and not flow features with small time/length scales which have very little effect on the loads.

	low blowing case	mid blowing case	high blowing case
freestream Mach number	0.10049	0.10057	0.10069
nozzle pressure ratio	1.08755	1.22330	1.30329
Reynolds number	488,000	487,000	508,800

Table 3: Details of the Mach and the Reynolds numbers, based on the chord length, for the wind tunnel experiments.[28]

B. Results

For the grid refinement study, see fig. 2 and table 4, only the k-ω turbulence model with the middle NPR was used. All the grids produce a similar C_p distribution with the finer grids predicting slightly lower suction over the coanda surface, fig. 2a. However, the surface pressures just after the slot are effected slighty by the level of refinement. The result of this is slightly lower upper surface velocities, a smaller leading edge suction peak and the stagnation point hasn't moved as far along the lower surface. For the medium and fine grids there is an unsteadiness in the CFD solution which is suggested in the lift coefficient, fig. 2b. This is most likely caused by the recirculation zone present just outside the lower sealed slot. The rest of the results presented will be with the coarse grid as the convergence rate is much better and the improvement in the solution is negligible using the finer grids.

For the integrated loads from the CFD results see table 4. There are no recorded loads aside from C_μ from the experimental data to compare with. However, in the experiment C_μ is estimated by assuming the pressure at the slot is the freestream pressure and using the isentropic relations, in equation 2, p_j is replaced by p_∞. Increasing the NPR causes a lower pressure at the slot, increasing the jet velocity and producing a larger discrepancy relative to the experimental C_μ's for the higher blowing cases.

For a comparison of the C_p distribution see fig. 3. At the lowest NPR the choice of turbulence model makes little difference to the result, fig. 3a. Both show good agreement with the experimental results with a slight over prediction of the suction on the upper surface and higher pressure on the lower surface. This could be due to the walls of the wind tunnels preventing the streamlines from curving around the aerofoil as much as they would in free air. At the middle NPR the SST model is predicting more suction over the coanda surface and this difference increases at the highest NPR. The k-ω model produces more eddy viscosity in

NPR	Turbulence Model	C_l	C_d	C_μ
low	k-ω	1.744	0.04365	0.05219
	SST	1.772	0.04285	0.05288
middle	k-ω (coarse grid)	3.631	0.07473	0.12186
	k-ω (extracoarse grid)	3.628	0.07752	0.12067
	k-ω (medium grid)	3.585-3.587	0.07093-0.07176	0.12167
	k-ω (fine grid)	3.555-3.565	0.06915-0.07097	0.12185
	SST	3.959	0.08243	0.12447
high	k-ω	4.490	0.09547	0.15729
	SST	5.093	0.11468	0.16263

Table 4: Integrated loads from the CFD results.

the shear layer between the jet and the freestream flow, fig. 4c. This speeds up the mixing process between the jet and surrounding flow causing it to separate at an earlier point on the trailing edge. As the jet remains attached longer with the SST model, this lowers the pressure over the rest of the surface which also has the secondary effect of increasing the C_μ as the velocity of the jet increases due to the pressure drop around the slot increasing the difference further. The k-ω model shows relatively good agreement with the experiment over the coanda surface but overpredicts the leading edge suction peak and the location of the stagnation point. Angle of attack corrections are available from the first set of results[17] which show that the discrepancy in these areas is mainly a result of the downwash caused by the high lift generated. However, a full 3D simulation including the wind tunnel walls is needed to quantify the exact effects of the walls and downwash.

For a comparison of the boundary layer velocity profiles see fig. 5 for the lowest NPR and fig. 6 for the middle NPR. Similarly to the C_p comparison at the lowest NPR both turbulence models show good agreement with a slight overprediction of the upper surface velocities and underprediction of the lower ones. This is likely due to the walls of the wind tunnel preventing the streamlines from curving as mentioned above. The effect of this is that the leading and trailing edge stagnation points are overpredicted. As a result of this the location where the velocity measurements were taken in the experiment are further away from the stagnation point on the lower surface and closer on the upper surface. This becomes more apparent with the middle NPR due to the higher lift produced the effect of the wind tunnel walls increases. Especially when seeing the difference between the two turbulence models, as the SST model is predicting the rear separation point further along the coanda surface the discrepancy is larger.

C. CC Validation Summary

From the CFD study, it can be seen that using PMB with current meshing techniques the flow physics of trailing edge CC devices can be predicted with reasonable accuracy. There are a few areas of the flow where there are discrepancies relative to the experimental data, such as at the leading edge the stagnation point's location and the suction peak is overpredicted. However, these discrepancies can be partly explained by experimental issues like the downwash caused by the high lift generated. An angle of attack correction for the first set of wind tunnel results has been obtained using a CFD method which accounts for this discrepancy. A 3D simulation could be used to quantify these discrepancies more precisely however as the aim is the application of these devices to a UCAV planform the level of agreement is adequate for these purposes. Another conclusion that can be drawn from this validation case is that the k-ω turbulence provides the best comparisons with the experimental data. This is due to the fact that the rear separation point predicted by k-ω is closer to the experimental one and this is one of the key features of these types of flows.

IV. UCAV Validation Test Case

The SACCON (Stability and Control Configuration) is a UCAV planform which will be used as a validation test case to demonstrate that the PMB code is capable of predicting vortical flowfields that are typically seen around UCAVs. It has a lambda wing with a sweep angle of 53° and a wing washout of 5°. The body has a length of $1.061m$, the chord at the root is $0.479m$, the half-span is $0.769m$ and the wing area is $0.77m^2$. New wind tunnel models including inboard and outboard flaps have been built which are being investigated within the AVT-201 task group.[29] These are referred to as the F19 which is used for low speed tests and has the dimensions mentioned above and the F17E which is about two and a half times smaller and is used for the high speed tests. See fig. 7 for a planform view of the SACCON with the locations of the pressure taps and the flaps in the experimental setup. The experimental data has been obtained from the low speed wind tunnel in Braunschweig[30] owned by the German-Dutch Wind Tunnels foundation.

A. Treatment of the Control Surfaces

Work has been done by Rampurawala at the University of Glasgow[31] on the treatment of control surfaces by structured multi-block solvers. This thesis investigated two of the possible options. Firstly, leaving the flap geometry as is and meshing the gap between the flap and the wing. Secondly, using a blending region between the wing and the flap to go from the trailing edge geometry of the wing to the flap geometry in a smooth fashion. In the work referenced this was done within the CFD solver as the flap geometry isn't given. In this work the second option is used as the first one results in extremely low quality cells, due to the skewness, in the gap, it increases the refinement required significantly and it reduces the convergence rate. However, one of the drawbacks of the second option is that the geometry is being approximated within the blending region. For the SACCON, as the flap geometry is known, the blending process was done during the grid generation process instead of within the solver. Between the flaps and the wings there is a gap of 1mm, this is surfaced over and is included in the blending region. The original flap surfaces are cut at either end by 25% of the flap chord and this is used as a blending region. Surfaces were then constructed within this region to obtain continuity between the wing and the flap in the spanwise direction. The effects of different size blending regions on the integrated loads and the convergence rate are investigated in.[32]

B. Grids and Computational Setup

A multi-block grid consisting of 260 blocks was generated using the ANSYS ICEM software package. The geometry was scaled using one metre as a unit length with the apex of the aircraft as the origin. The topology for the surface of the SACCON, see fig. 9a, was chosen so that each flap surface would be represented by a block face. This is done so that each flap can be deflected separately within the CFD code, i.e. deploying a flap during an unsteady calculation. As a result of this there is no block edge associated with the surface discontinuity in the wing, which is therefore approximated by the cells it passes through. The grid has a C-topology at the leading edge, see fig. 9c and an O-topology at the wing tip, see fig. 9b. The farfield is approximately 20 chord distances away from the aircraft in every direction with a first cell spacing normal to surface of $c_{ref} \times 10^{-5}$. There are 124 cells in the chordwise direction, both upper and lower surfaces, and 488 cells in the spanwise direction with a total of just over 14 million cells. The grid density and expansion ratios in the chordwise, spanwise and normal directions were based on a grid built by Vallespin which was used for earlier work on this configuration.[25,33] A grid refinement study was performed as part of this work demonstrating that this level of refinement provides a good compromise between accuracy in terms of the aerodynamic loads and the computational time required to achieve a converged solution.

The wind tunnel conditions for the experiments were a Mach number of 0.145 and a Reynolds number based on the reference chord of 1.585×10^6. The turbulence model used was the k-ω with vortex correction, chosen based on the previous work.[33] This limits the production of turbulent kinetic energy in regions of high vortical flow and increases the production of the dissipation rate to try and correct the amount of turbulent kinetic energy produced in the vortex core. The purpose of this is to improve the accuracy of the CFD solution at the higher angles of attack where vortex structures dominate the flow.

C. Results

For a qualitative understanding of the vortex structures that occur in the CFD solution as the angle of attack is increased, see fig. 10. These are identified using the λ_2 criterion, a vortex identification technique

developed by Jeong and Hussain.[34] A short description of the flow structure for this UCAV planform will follow, for more detail the reader is directed to.[25,26] As the angle of attack is increased the wing tip vortices increase in size, this can be seen between figs. 10a and 10b. Further increase in the angle of attack results in the onset point of the wing tip vortex moving inboard along the leading edge and vortices on either side of the body originating from the sharp nose become apparent. As the vortex moves inboard it starts to reduce the area of attached flow over the wing, fig. 10c. Eventually the vortices break down and the flow over the entire wing becomes separated, fig. 10d.

For the comparison of the computational and experimental integrated loads see fig. 11. The lift coefficient, fig. 11a, shows relatively good agreement for the attached part of the flow. In the non-linear region the computed lift shows a similar trend to the experiments, increasing lift with a reduction in slope. However, the lift stops increasing at approximately 24° whereas the CFD predicts a continued increase. Similarly the drag coefficient, fig. 11b, shows good agreement until the flow separates. There is a slight underprediction between 16° and 18°, however, the agreement between the computational and experimental results improves again after this. This could be due to the fact that the surface discontinuity is being approximated and it is the point in the flow where the wing tip vortex is passing over it, see figs. 10b and 10c. For the pitching moment coefficient, fig. 11c, the lack of a sting causes a discrepancy in both the attached and separated regions of the flow. Work has been done[26] to demonstrate that the inclusion of the sting accounts for this discrepancy. Also the initial dip at 16° is not captured by the CFD however the pitching moment does**flatten out in this region**. This is probably for the same reason as for the difference observed in the drag coefficient.

For the comparison of the surface pressures see fig. 12. The CFD shows good agreement with the experimental results in the attached regime of the flow. The pressure coefficients on the upper surface are slightly underpredicted. As the angle of attack increases and the vortices increase in strength the difference between the computational and experimental results becomes more evident. Particularly in the areas beneath the vortices, see figs. 12c and 12e between -0.16 and -0.12 on the 20% slice and between -0.3 and -0.2 on the 45% slice. These differences are partly due to the unsteady nature of the flow and the sting not being modelled. Inclusion of these aspects has been shown to increase the agreement in those areas.[26]

D. UCAV Validation Summary

The computed aerodynamic loads from the CFD simulations show good agreement with the loads recorded in the wind tunnel experiments during the attached regime of the flow. There are a few discrepancies, such as the offset observed in the pitching moment coefficient throughout the angle of attack range. However, previous work done on this configuration has shown that the sting used to mount the model in the wind tunnel is responsible for these discrepancies. At the higher angles of attack where the vortices start to dominate the flow larger differences are seen between the experiment and computations. This is attributed mainly to RANS methods not being able to capture the unsteady nature of the flow and the behaviour of the vortices accurately as has been shown in previous work done on the configuration. Further investigations of the effects of using different turbulence models and URANS for the SACCON with the conventional control surfaces have been conducted as shown in ref.[32]. An important point to make, is that the flow topology is predicted correctly throughout the angle of attack range and this is key in determining whether the circulation control will be effective. Therefore, the accuracy obtained is sufficient to get an understanding of whether the fluidic devices will be effective in providing control moments for such aircraft in the attached flow regime.

V. SACCON with Trailing Edge Circulation Control

The CAD model of the DLR-F19 is used as the basis for the CC modifications. The spanwise extent of the trailing edge CC device is the same as the inboard and outboard flaps. The trailing edge of the entire model has been modified to allow for an O-grid topology, which will increase the grid quality around the coanda surface. The modifications to the body are done by creating a semi-circular trailing edge and matching the gradients with the existing blunt trailing edge, see fig. 13a.

The modifications to the wings are done by truncating the existing wings at the required thickness and creating a semi-circular trailing edge with upper and lower slots. A coanda radius of 0.5% and a coanda radius to slot height ratio of 10, following the suggestions of S. Michie,[35] and were tested on a 2D aerofoil section of the SACCON to confirm they were appropriate. For the parts of the wings which are not employing the

fluidic devices, the trailing edge is modified in a similar way to that of the body. At the junction between the wing and body the original surface between the body and the wing is cut to create a smooth transition from the trailing edge thickness at the body to the thickness required for the CC device, see fig. 13b. A second configuration consisting of three slots, of equal width, on either wing instead of one was also constructed. This was done by creating two zero thickness walls within the plenum chamber, to split it into three separate sections. Having a wall with a thickness significantly increases the number of points needed in the spanwise direction to prevent the grid from expanding too rapidly. Therefore, this is done to try and maintain the grid at a reasonable size. The purpose of this is an alternate way to control the roll moment generated instead of varying the NPR, as the efficiency ($\frac{\partial C_l}{\partial C_\mu}$) of the device is not constant across the NPR. Each slot can be turned on individually and to increase the C_μ multiple slots can be used at once. Therefore the middle slot will be turned off and the outer two will be used to determine if there may be potential interference. The slots will be referred to as IB, MB and OB from root to tip respectively.

A. Grid and Computational Setup

The grid for the SACCON with the CC device uses the same number of cells in chordwise, spanwise and normal directions as for the F19. At the trailing edge the refinement has been chosen based on experience with the two dimensional CFD validation. The grids for the single slot and three slot configuration have a total of 12.68 and 16.29 million cells respectively. The refinement, in the 3 slot case, is added only in the spanwise direction, to the blocks along the span where the CC is being employed. This is done by using the same expansion ratio and wall spacing that is used at either end of the slot, in the single slot case, at the two zero thickness walls. The Mach and Reynolds numbers were kept the same as the wind tunnel experiments, 0.145 and 1.585×10^6 respectively, to allow for a comparison with the experimental data with the flaps deployed. The NPR was chosen by running a coarse version of the grid (coarse version has every other grid point in each direction removed) at a range of NPR's to determine what roll moment could be achieved. An NPR of 1.2 was chosen based on this which was then used with the fine version of the grid, this corresponds to a C_μ of 0.00645 at 0° for the single slot case. The same NPR was used with the three slot configuration, corresponding to a C_μ of 0.00424. It is important to use the same NPR, as the efficiency depends quite significantly on this parameter.

B. Results

To get an understanding of how the trailing edge CC device effects the flowfield around the trailing edge see fig. 14. As we are investigating the roll actuation, at an angle of attack of zero, the flow over the left wing is almost a reflection of the right wing. There are a few differences but the overall flow behaviour is similar. Therefore, the flow will be described for the right wing, for the left wing the upper and lower surfaces are swapped. The sides of the jet sheet exiting the slot are slowed down by the side walls of the CC device, see fig. 14b. These parts of the jet interact with the oncoming flow creating vortices at the root and tip of the CC device. Beneath this at the root there is a recirculation zone which interacts with the jet and oncoming flow to create another vortex, see fig. 15a. This travels along the lower surface of the trailing edge initially increasing in size and then combining with the wing tip vortex, figs 16a,17a,22a and 22b. On the right wing the result of this is a decrease in the size of the wing tip vortex as they are counter-rotating and vice versa for the left wing. As the jet exits normal to the trailing edge it creates a strong shear layer with the oncoming flow beneath the wing forming another vortex towards the center of the CC device, figs 16a, 22a and 22b. For the three slot configuration the vortex originating from the root of the wing on the lower surface mixes with the oncoming flow in the middle section, as the jet is not in use here, see fig. 22d. Then another vortex originates from the start of the outboard jet and similarly to the single slot case travels along the span and combines with the wing tip vortex. This increases the number of vortices emanating from the trailing edge but reduces the size of them.

For the integrated loads see fig. 18. The CFD captures the contribution to the integrated loads from the deflected flaps accurately. This can be seen most clearly from the roll moment, fig. 18d, which is zero in the attached flow regime for the undeflected case. There are some discrepancies in the integrated loads, however, similarly to the undeflected case these are caused by not modelling the sting in the CFD and not being able to capture the behaviour of the vortices accurately at high angles of attack. For any subsequent comparisons between the CC and flaps the CFD results are used. Initially, The performance of the CC relative to flaps will be discussed, then a comparison of the single slot configuration and the three slot configuration with the

OB/IB slots in use. Finally, A discussion of how the flow topology effects the control moments generated by the CC.

As can be seen from fig. 18d the roll moment of the CC device exceeds that of the flap at an angle of attack of zero. The focus of this work is to understand how the devices will work and whether they will be effective accross the angle of attack range on such a planform. Matching the initial roll moment did not seem necessary for this as long as it was relatively similar, so the NPR was left at 1.2 for the entire range. As can be seen from the lift, drag and pitching moment coefficients, figs. 18a, 18b and 18c, the CC device has a relatively similar effect on these coefficients as the flaps do. The pitching moment coefficient's gradient is slightly higher than the flaps causing a larger pitch up moment as the angle of attack is increased. This is most likely due to the CC device causing a large pressure drop around the trailing edge which affects the flow in its vicinity. Whereas for the flaps the pressure change spreads over the rest of the wing more evenly. The gradient of the lift coefficient curve as well as C_L values have been reduced slightly due to the reduced wing area, the original wing area is used for scaling the coefficients. The CC device produces slightly more drag at the lower angles of attack however the difference is reduced as the angle of attack is increased. The rolling moment slope for the CC device is lower than the conventional flaps for the lower angles of attack, maintaining a stronger roll moment initially. However, it starts to increase after 10° making the CC device's effectiveness significantly impaired at higher angles where as the conventional flaps have an almost linear loss of roll moment with spikes in the non-linear region.

There are few visible differences between the single slot configuration and the three slot configuration with the OB/IB slots in use when looking at the integrated loads. The drag and pitching moment are slightly lower at the low angles of attack but that is expected as the jet is only active over two thirds of the region in the three slot case. Also the loss of roll moment over the angle of attack range occurs in a very similar manner. The key difference between them can be seen when we look at the efficiency of the CC, see fig. 18e. The three slot configuration is between 6.5% and 12% more efficient during the attached regime, possible reasons for this will be discussed in the next paragraphs.

For an understanding of the way the moment is generated and why the effectiveness of the trailing edge CC deteriorates quickly at the higher angles of attack see fig. 19. These plots show the moment generated as a proportion of the total roll moment, it is calculated by determining the moment at each point on the surface and dividing by the total moment. The main portion of the rolling moment is generated on the upper surface in the area around the slot while the upper slot is in use and vice versa while the lower slot is being used, figs. 19a and 19b. There is a large suction peak at the slot which lowers the pressure in the area around it on the upper surface. The moment contribution increases towards the wing tip, partly for the obvious reason that it is further from the moment reference point but also because the pressure is lower there, increasing the speed of the jet and making it more effective. The vortex emanating from the root of wing on the opposite side of the jets counteracts the moment, however this also blocks the flow creating a higher pressure region that also contributes to the moment, see the trailing edge of the left wing in fig. 19a. Visually it seems that the vortex is having a slighlty stronger effect than the high pressure region. However, it is very difficult to show this concretely as it is unclear how to define the boundaries of the two regions. As the angle of attack is increased and the vortices start to dominate the flow over the upper surface, the area which is generating the majority of the moment starts to shrink, see figs. 19c, 19d. Also as a proportion of the total moment the flow around the leading edge (which is affected mainly by the angle of attack and not the jet) contributes much more relative to the effects of the jet. The location of the vortices is affected slightly by the pressure change around the trailing edge, fig. 22c, which decreases the rate of loss of roll moment. However, this does not compensate enough for the reduction in moment contribution around the slot. As the flow separates across the entire upper surface of the wing the coanda jet completely loses its effectiveness and by 21° provides almost no roll moment whatsoever.

For the three slot configuration with the OB/IB slots in use the effects of the OB and IB jets spill over into the middle section of the wing lowering the pressure in that region too. This is probably the major reason for the difference in the efficiency between the single and three slots configurations. Another potential reason is the difference in the behaviour of the vortices that travel along the surface opposite the active jet. They are significantly smaller and it could be that this with the combination of the high pressure regions that they cause are generating more of the moment. These effects are most likely the cause of the difference in the efficiency between the single and three slot configurations.

VI. Conclusions and Future Work

Two validation cases have been simulated, The CC-E0020EJ aerofoil and the SACCON. The results have demonstrated that the PMB code can predict the flow physics for coanda jets and vortical flowfields. Two turbulence models were tested for the coanda jet with the k-ω model providing the best comparisons with the experimental results. For the SACCON slight discrepancies with both the loads and surface pressures occur at the low angles of attack. However, these have been shown, in other works, to be caused by not including the sting and the wind tunnel walls in the CFD simulation. In the non-linear regime of the flow the RANS methods fail to capture the behaviour of the vortices accurately. Higher fidelity turbulence modelling and use of the URANS equations has been shown to improve the agreement at the high angles of attack.

A comparison of a generic UCAV's ability to produce roll moment using trailing edge CC with a single and three slot configuration and conventional mechanical surfaces has been conducted. The results have shown that at low of angles of attack the fluidic devices can produce similar roll moments to flaps. Also initially as the angle is increased the loss of roll moment is lower for the CC. However, it relies mainly on the upper surface of the wing to generate the control moment. At high angles of attack the flow separates over the wings and by 21° the CC devices are almost completely ineffective. Where as for the flaps both upper and lower surfaces contribute to the moment and they retain their effectiveness up to higher angles of attack. The key difference between the single slot and three slot configuration was in the efficiency of the CC. The three slot configuration was approximately 10% more efficient between angles of attack of 0° and 15°. This is attributed to the spill over effect around the slot and the reduced size of the vortex on the opposite surface.

Further investigation into the number of slots should be done to see if the efficiency can be increased further. A parametric study of the distance between each of the slots, the number of slots and the width of each slot could be performed to determine this. However, with the methods used in this paper this task would require a very large amount of both human labour and processor hours. This is because a new grid, both the physical geometry and the block structure, would need to be modified whenever the parameters are changed.

Further work also needs to be done on the dynamic behaviour of the CC devices. This would involve unsteady simulations to calculate the time it takes for the coanda jet to become attached and forced oscillations to determine how much hysteresis there is. Tabular methods can then be developed for manoeuvre prediction, this will make it possible to determine the control settings required to achieve a required manoeuvre. Comparisons with time-accurate CFD calculations can then be performed to demonstrate if these methods are suitable for predicting the aerodynamic loads and moments during unsteady manoeuvres. Also this would make it possible to determine whether or not the devices are suitable as a roll effector for UCAVs.

Acknowledgments

The authors are grateful for the financial support provided by the Engineering and Physical Sciences Research Council (EPSRC) and BAE Systems. We would like to thank Dr. Gregory S. Jones and Mr. Keith B. Paschal for providing us with the website to access the wind tunnel results relating to the circulation control aerofoil, CC-E0020EJ. We would also like to thank all the members of the AVT-201 group for all the data and wind tunnel results relating to the SACCON.

References

[1]Englar, R., "Circulation Control for High Lift and Drag Generation on STOL Aircraft," *Journal of Aircraft*, Vol. 12, No. 5, 1975, pp. 457–463.

[2]Englar, R., "Design of the Circulation Control Wind STOL Demonstrator Aircraft," *Journal of Aircraft*, Vol. 18, No. 1, 1981, pp. 51–58.

[3]Loth, J. and Fanucci, J., "Flight Performance of a Circulation Controlled STOL Aircraft," *Journal of Aircraft*, Vol. 13, No. 3, 1976, pp. 169–173.

[4]Englar, R., "Development of the A-6/Circulation Control Wing Flight Demonstrator Configuration," Tech. rep., DTIC Document, 1979.

[5]Loth, J. and Boasson, M., "Circulation Controlled STOL Wing Optimisation," *Journal of Aircraft*, Vol. 21, No. 2, 1984, pp. 128–134.

[6]Jones, G., Viken, S., Washburn, A., Jenkins, L., and Cagle, C., "An Active Flow Circulation Controlled Flap Concept for General Aviation Aircraft Applications," *1st Flow Control Conference, St. Louis, Missouri*, 24-26 June, 2002.

[7]Cagle, C. and Jones, G., "A Wind Tunnel Model to Explore Unsteady Circulation Control for General Aviation Applications," *The 22nd AIAA Applied Aerodynamics Conference, St. Louis, Missouri*, 24-26 June, 2002.

[8]Crowther, W., "Towards Integrated Design of Fluidic Flight Controls for a Flapless Aircraft," *The Aeronautical Journal*, Vol. 113, No. 1149, 2009, pp. 699–713.

[9]Cook, M., Buonanno, A., and Erbsloh, S., "A Circulation Control Actuator for Flapless Flight Control," *The Aeronautical Journal*, Vol. 112, No. 1134, 2008, pp. 483–489.

[10]Wilde, P., Crowther, W., and Harley, C., "Application of Circulation Control for Three-Axis Control of a Tailless Flight Vehicle," *Proceedings of the Institution of Mechanical Engineers, Part G: Journal of Aerospace Engineering*, Vol. 224, No. 4, 2010, pp. 373–386.

[11]Tao, T., Kidwell, G., and Vanderplaats, G., "Numerical Optimization of Circulation Control Airfoils," *Journal of Aircraft*, Vol. 19, No. 2, 1982, pp. 145–150.

[12]Shrewsbury, G., "Numerical Study of a Research Circulation Control Airfoil Using Navier-Stokes Methods," *Journal of Aircraft*, Vol. 26, No. 1, 1989, pp. 29–34.

[13]Jones, G. and Joslin, R., "Proceedings of the 2004 NASA/ONR Circulation Control Workshop," 16-17 March, 2004.

[14]Abramson, J., "Two-Dimensional Subsonic Wind Tunnel Evaluation of Two Related Cambered 15-percent-thick Circulation Control Airfoils," Tech. rep., DTIC Document, 1977.

[15]Chang III, P., Slomski, J., Marino, T., Ebert, M., and Abramson, J., "Full Reynolds-Stress Modeling of Circulation Control Airfoils," *Reston, VA: American Institute of Aeronautics and Astronautics*, 2006, pp. 445–466.

[16]Paterson, E., Baker, W., Kunz, R., and Peltier, L., "RANS and Detached-Eddy Simulation of the NCCR Airfoil," *Computer Architecture, Proceedings. 31st Annual International Symposium on*, 2004.

[17]Englar, R., Jones, G., Allan, B., and Lin, J., "2-D Circulation Control Airfoil Benchmark Experiments Intended for CFD Code Validation," *47th AIAA Aerospace Sciences Meeting Including The New Horizons Forum and Aerospace Exposition, Orlando, Florida*, 5-8 January, 2009.

[18]Rumsey, C. and Nishino, T., "Numerical Study Comparing RANS and LES Approaches on a Circulation Control Airfoil," *International Journal of Heat and Fluid Flow*, Vol. 32, No. 5, 2011, pp. 847–864.

[19]Allan, B., Jones, G., and Lin, J., "Reynolds-Average Navier-Stokes Simulation of a 2D Circulation Control Wind Tunnel Experiment," *AIAA Paper*, Vol. 25, 2011, pp. 2011.

[20]Cummings, R. and Schutte, A., "An Integrated Computational/Experimental Approach to UCAV Stability & Control Estimation: Overview of NATO RTO AVT-161," *28th AIAA Applied Aerodynamics Conference*, 2010.

[21]Loeser, T. and Vicroy, D., "SACCON Static Wind Tunnel Tests at DNW-NWB and 14'x22' NASA LaRC," *28th AIAA Applied Aerodynamics Conference*, 2010.

[22]Vicroy, D. and Loeser, T., "SACCON Forced Oscillation Tests at DNW-NWB and NASA Langley 14x22-foot Tunnel," *28th AIAA Applied Aerodynamics Conference*, 2010.

[23]Gilliot, A. and Morgand, S., "Static and Dynamic SACCON PIV tests Part I: Forward Flowfield," *28th AIAA Applied Aerodynamics Conference*, 2010.

[24]Konrath, R., Roosenboom, E., Schroder, A., Pallek, D., and Otter, D., "Static and Dynamic SACCON PIV Tests Part II: Aft Flow Field," *28th AIAA Applied Aerodynamics Conference*, 2010.

[25]Vallespin, D., Da Ronch, A., and Badcock, K., "Validation of Vortical Flow Predictions for a UCAV Wind Tunnel Model," *28th AIAA Applied Aerodynamics Conference*, 2010.

[26]Jirásek, A. and Cummings, R., "SACCON Static and Dynamic Motion Flow Physics Simulations Using COBALT," *29th AIAA Applied Aerodynamics Conference*, 2010.

[27]Badcock, K., Richards, B., and Woodgate, M., "Elements of Computational Fluid Dynamics on Block Structured Grids Using Implicit Solvers," *Progress in Aerospace Sciences*, Vol. 36, No. 5, 2000, pp. 351–392.

[28]Paschal, K., Neuhart, D., Beeler, G., and Allan, B., "Circulation Control Model Experimental Database for CFD Validation," *50th AIAA Aerospace Sciences Meeting, Nashville, Tennessee*, 9-12 January, 2012.

[29]Cummings, R. and Schutte, A., "The NATO STO Task Group AVT-201 on 'Extended Assessment of Stability and Control Prediction Methods for NATO Air Vehicles'," *32nd AIAA Applied Aerodynamics Conference*, 2014.

[30]Huber, K., Vicroy, D., Schutte, A., and Huebner, A., "UCAV Model Design and Static Experimental Investigations to Estimate Control Device Effectiveness and S&C Capabilities," *32nd AIAA Applied Aerodynamics Conference*, 2014.

[31]Rampurawala, A., *Aeroelastic Analysis of Aircraft with Control Surfaces Using CFD*, Ph.D. thesis, University of Glasgow, 2006.

[32]Kennett, D., Hoholis, G., and Badcock, K., "Numerical Simulation of Control Surface Deflections over a Generic UCAV configuration at Off-design Flow Conditions," *32nd AIAA Applied Aerodynamics Conference*, 2014.

[33]Vallespin, D., *Development of a Process and Toolset to Study UCAV Flight Mechanics using Computational Fluid Dynamics*, Ph.D. thesis, University of Liverpool, 2011.

[34]Jeong, J. and Hussain, F., "On the Identification of a Vortex," *Journal of Fluid Mechanics*, Vol. 285, 1995, pp. 69–94.

[35]Michie, S., *A Design Methodology for Circulation Control Manoeuvre Effectors*, Ph.D. thesis, University of Manchester, 2008.

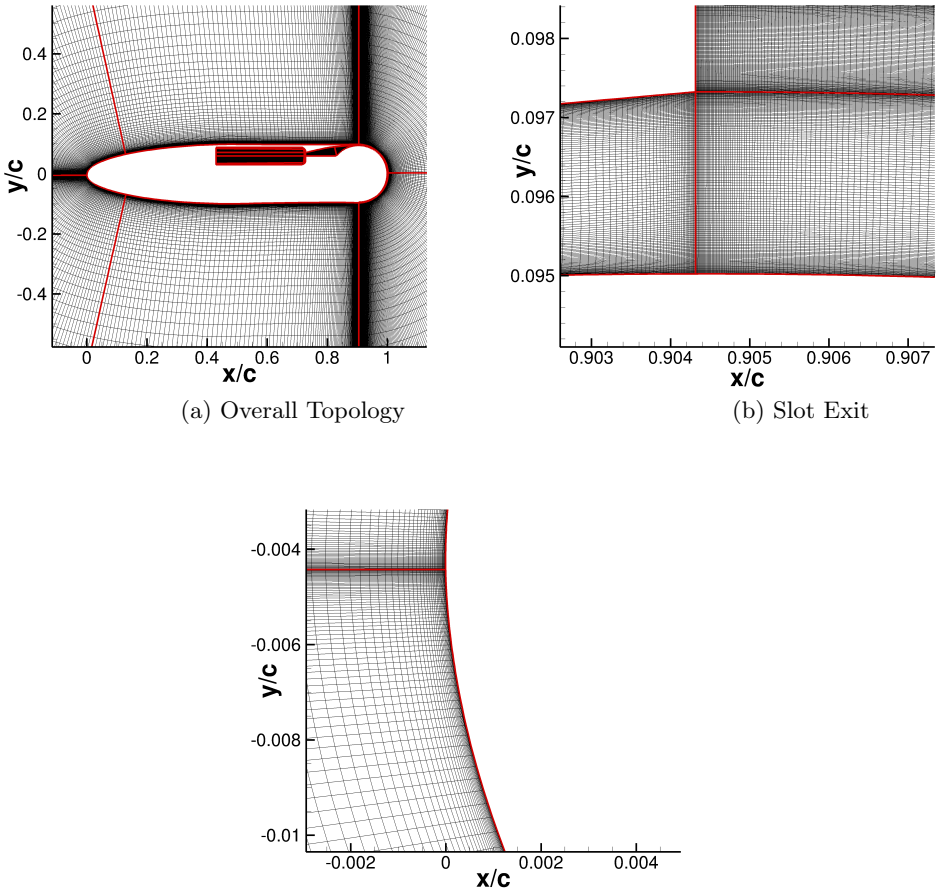

(a) Overall Topology

(b) Slot Exit

(c) Leading Edge

Figure 1: The finest grid used for the CC-EE0020EJ with close-ups of some key locations.

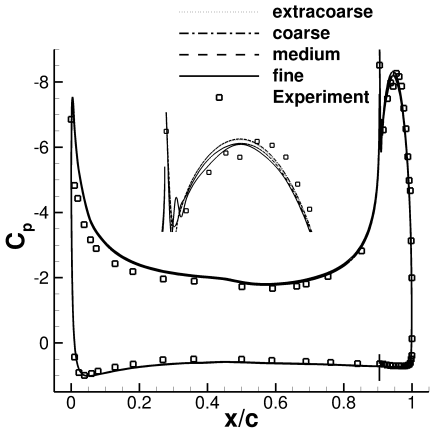

(a) C_p comparison with close-ups of the suction peak over the coanda surface.

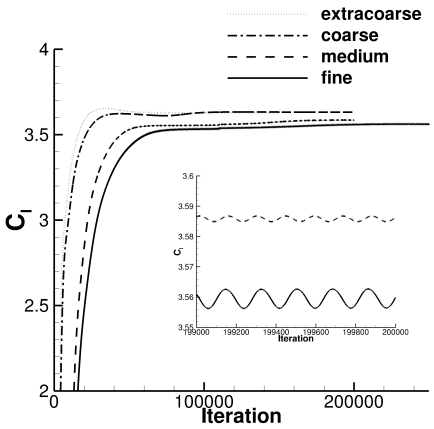

(b) C_l comparison.

Figure 2: Comparison of the C_p over the surface and the C_l for the grid refinement study for the CC-E0020EJ at a Mach number of 0.1 and a Reynolds number of half a million.

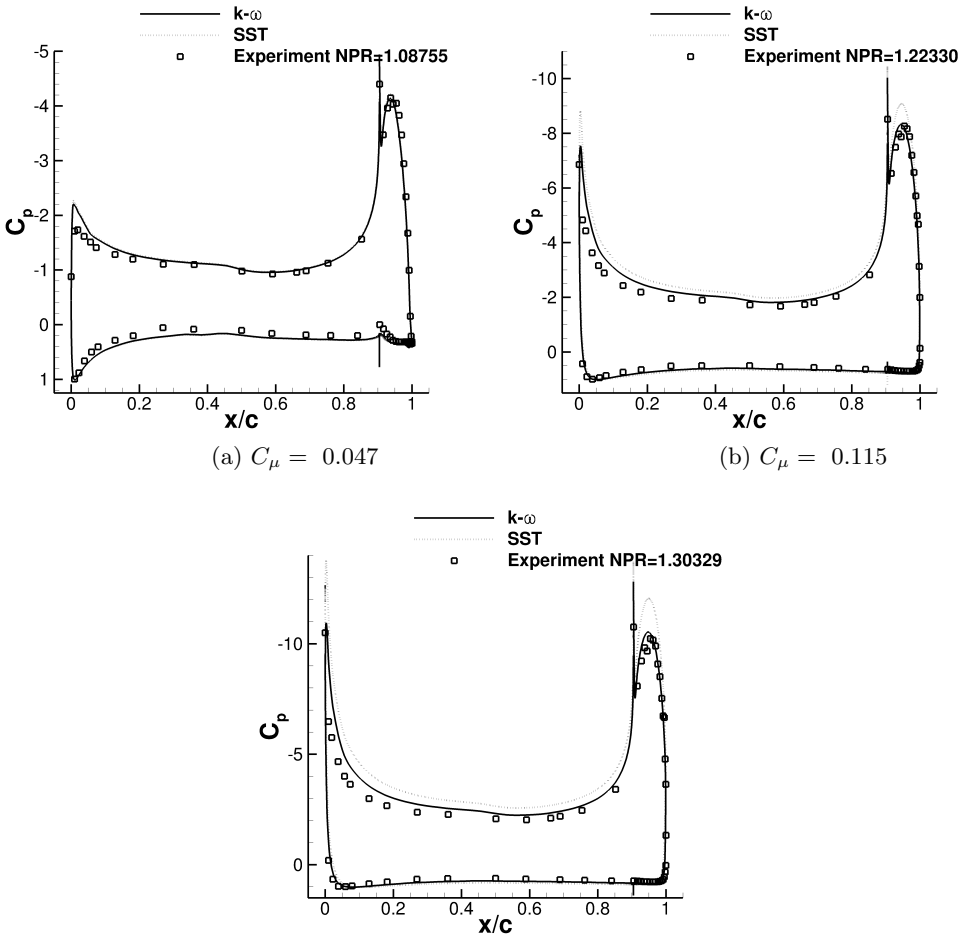

(a) $C_\mu =$ 0.047

(b) $C_\mu =$ 0.115

(c) $C_\mu =$ 0.150

Figure 3: Comparison of C_p from the CFD calculations and the experimental results[28] for the CC-E0020EJ at a Mach number of 0.1 and a Reynolds number of half a million.

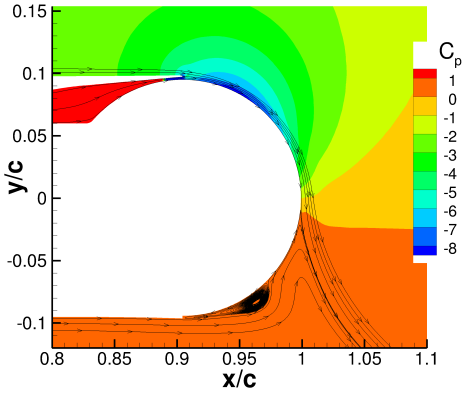

(a) Streamlines on C_p contours for NPR=1.22330 with the k-ω turbulence model.

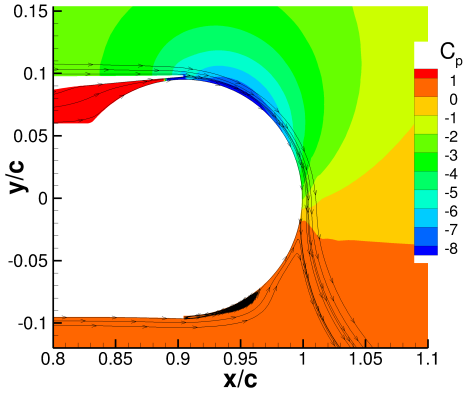

(b) Streamlines on C_p contours for NPR=1.22330 with the SST turbulence model.

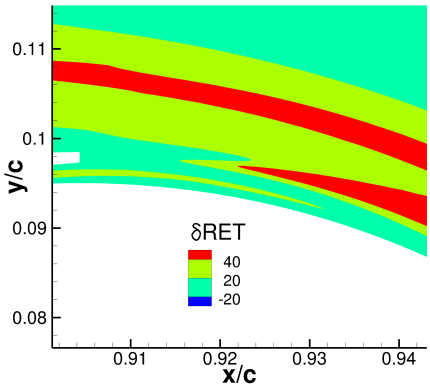

(c) Difference in the eddy viscosity levels between the k-ω and the SST turbulence models around the slot.

Figure 4: Comparison of two turbulence models for the CC-E0020EJ at a Mach number of 0.1 and a Reynolds number of half a million.

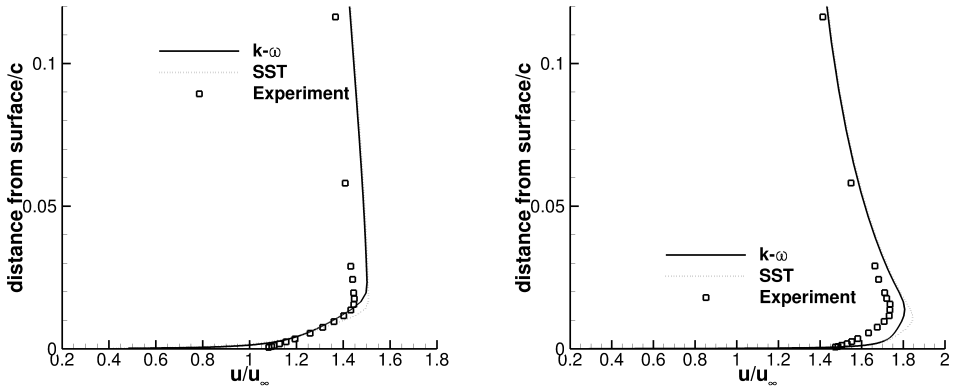

(a) Upper Surface $x/c = 0.8$

(b) Upper Surface $x/c = 0.9$

(c) Lower Surface $x/c = 0.8$

(d) Lower Surface $x/c = 0.9$

Figure 5: Comparison of boundary layer velocites from the CFD calculations and the experimental results for $C_\mu =$ 0.047 for the CC-E0020EJ at a Mach number of 0.1 and a Reynolds number of half a million.

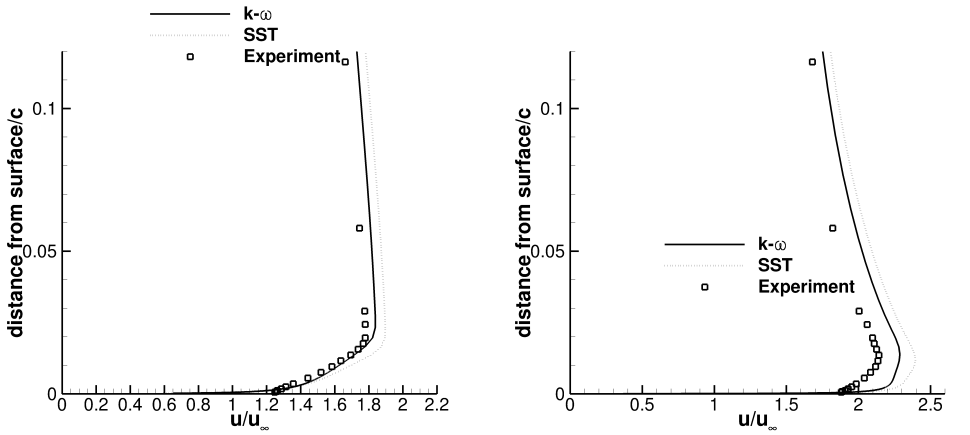

(a) Upper Surface $x/c = 0.8$

(b) Upper Surface $x/c = 0.9$

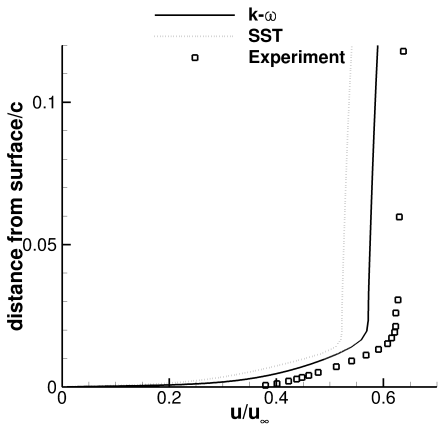

(c) Lower Surface $x/c = 0.8$

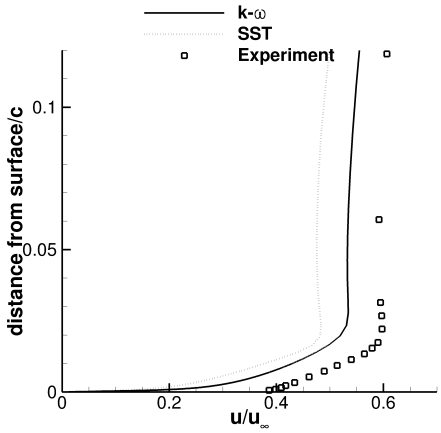

(d) Lower Surface $x/c = 0.9$

Figure 6: Comparison of boundary layer velocites from the CFD calculations and the experimental results for $C_\mu =$ 0.115 for the CC-E0020EJ at a Mach number of 0.1 and a Reynolds number of half a million.

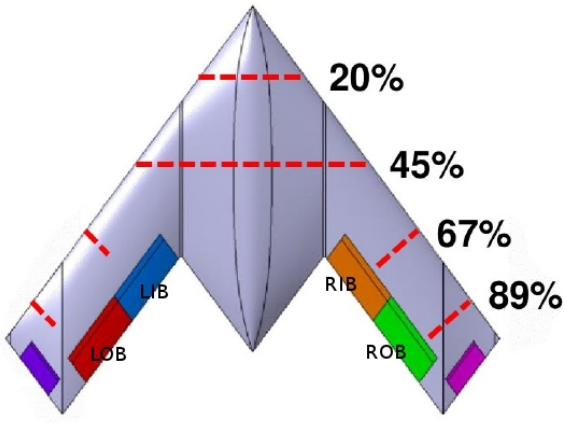

Figure 7: Top view of the SACCON with the locations of the pressure taps on the wind tunnel model.

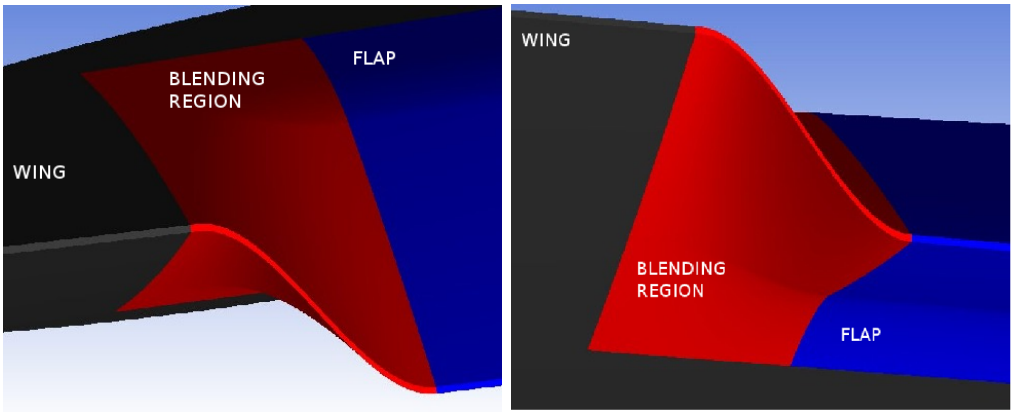

Figure 8: Screenshot of the region between the wing and flap used as a blending region for the SACCON with conventional control surfaces.

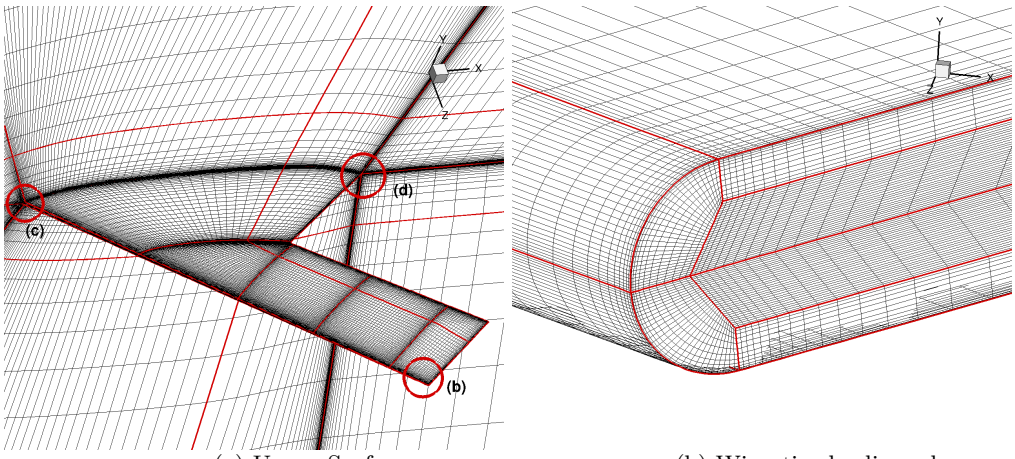

(a) Upper Surface

(b) Wing tip- leading edge

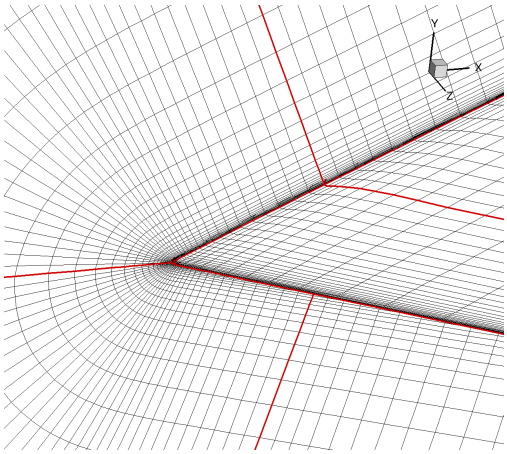

(c) Apex- leading edge

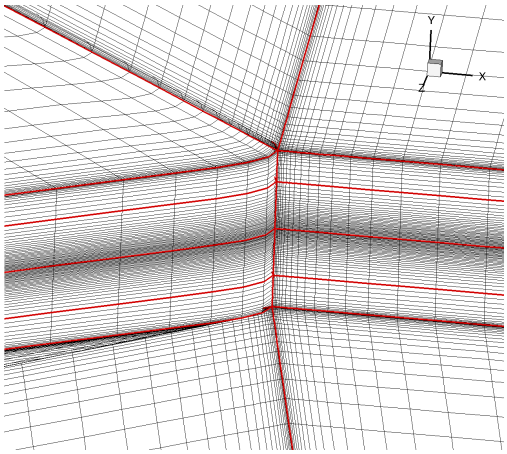

(d) Trailing edge

Figure 9: Grid topology at key locations for the SACCON.

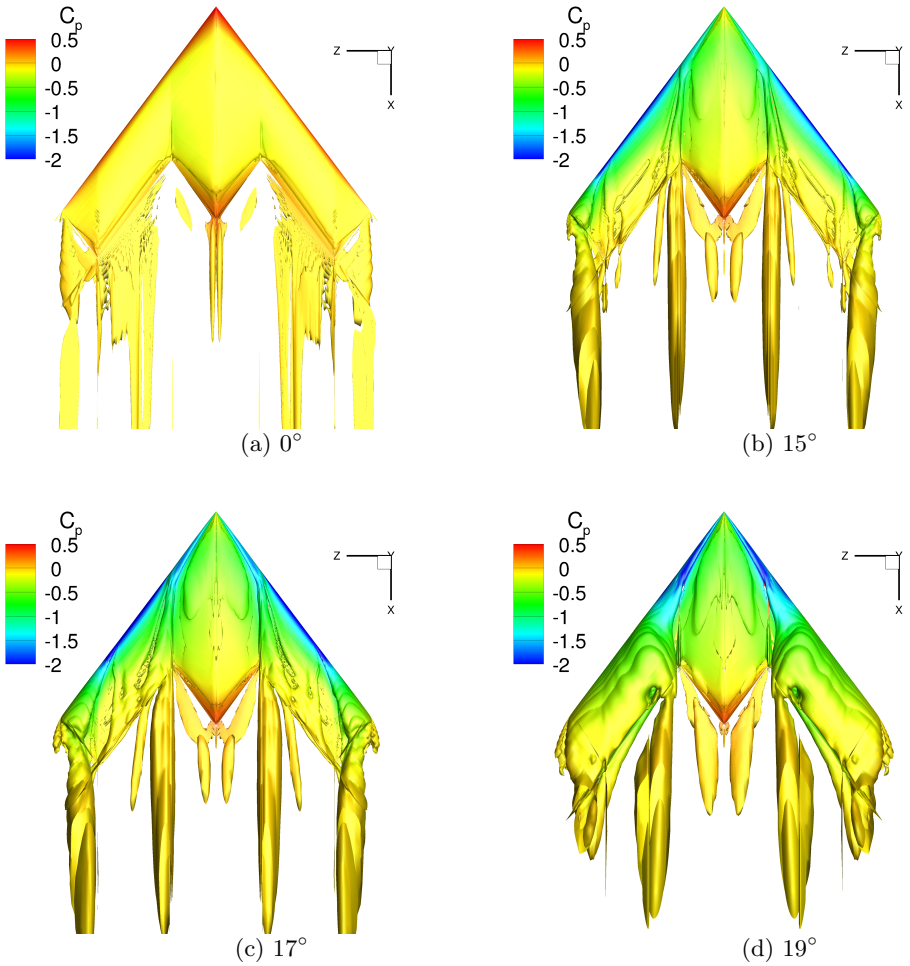

(a) 0° (b) 15°

(c) 17° (d) 19°

Figure 10: Iso-surfaces of the λ_2 criterion coloured with C_p for the SACCON at various angles of attack.

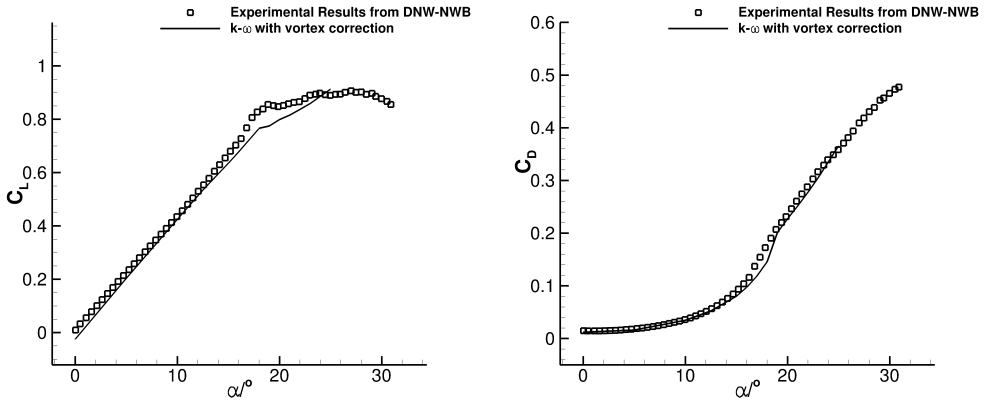

(a) Lift Coefficient

(b) Drag Coefficient

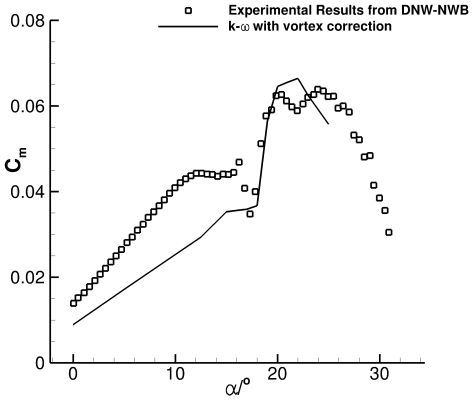

(c) Pitching Moment Coefficient

Figure 11: Comparison of the computational and experimental integrated loads for the SACCON.

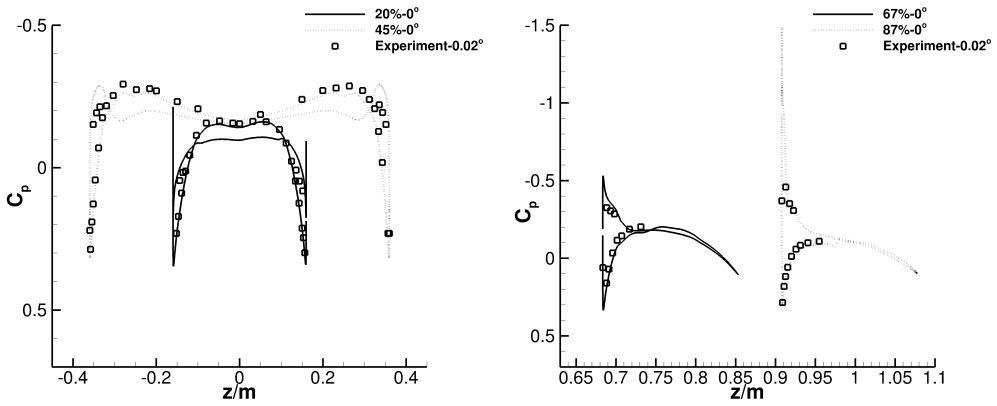

(a) 0°-body

(b) 0°-wing

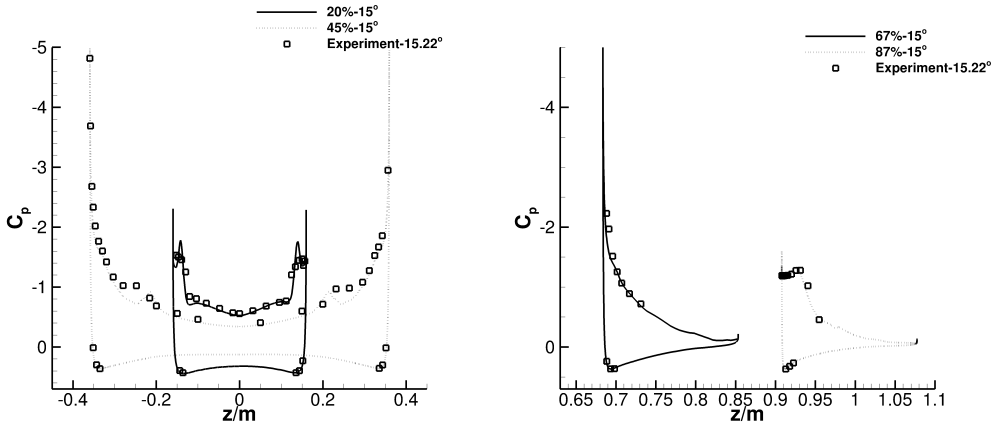

(c) 15°-body

(d) 15°-wing

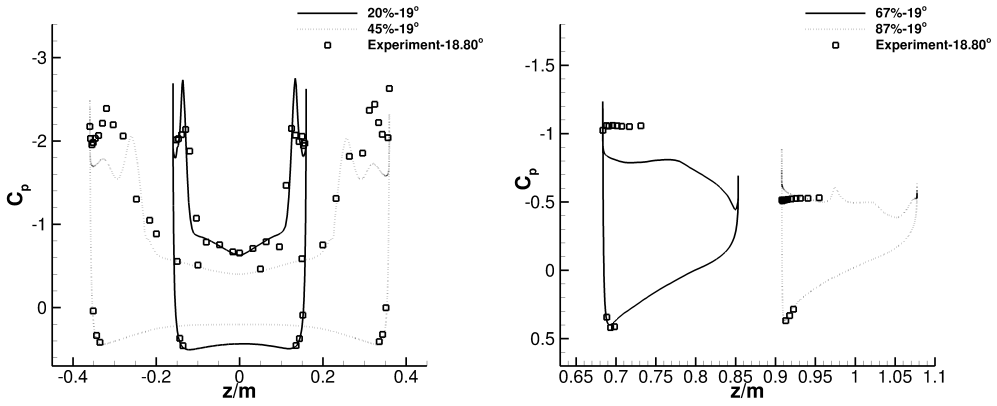

(e) 19°-body

(f) 19°-wing

Figure 12: Comparison of the computational and experimental surface pressure distributions for the SACCON.

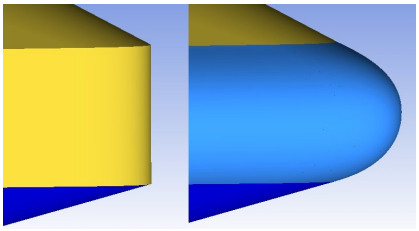

(a) The trailing edge of the body of the SACCON before and after the modifications are made.

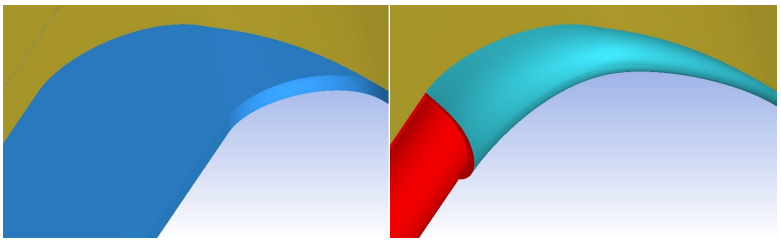

(b) The junction between the wing and the body of the SACCON before and after the modifcations are made.

Figure 13: Views of two key locations of the SACCON's trailing edge to show the modifications made for the CC device.

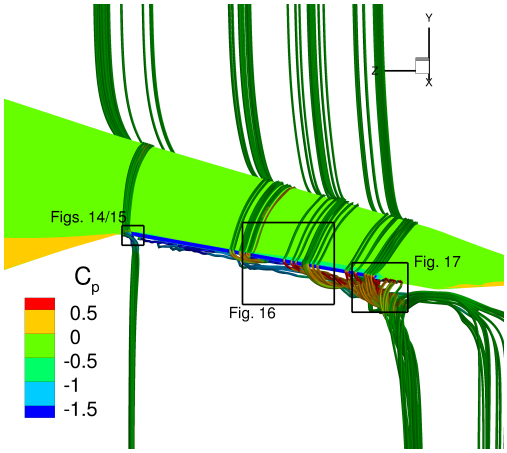

(a) Overall 3D view of the right wing with rectangles indicating where the close ups are.

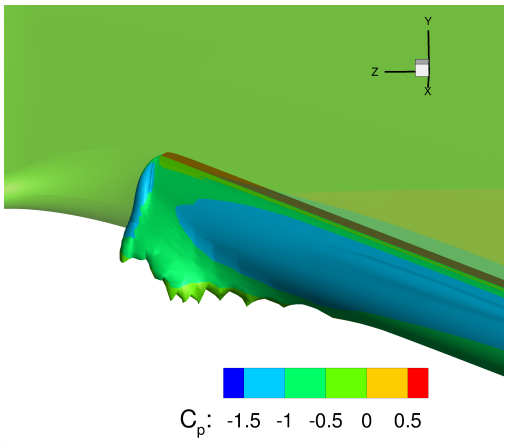

(b) 3D view at the root of the wing of the jet exiting the slot.

Figure 14: 3D view of the SACCON employing the circulation control on the right wing. The surfaces in the 3D views are coloured using C_P contours and the streamtraces are coloured with X vorticity.

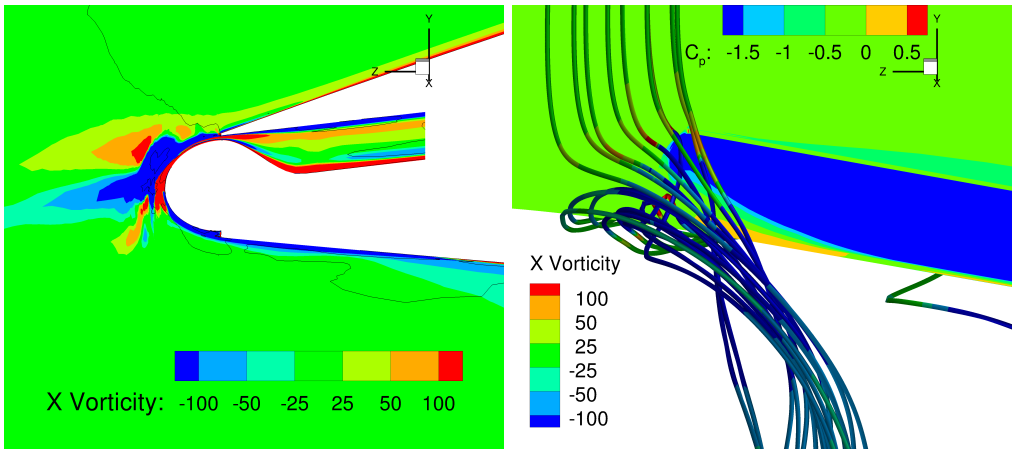

(a) Slice at x=0.772. (b) 3D view.

Figure 15: Slice and 3D view from the root of the SACCON's right wing. The slice has been coloured using X-vorticity contours and the regions enclosed by black lines are regions identified as vortices by the λ_2 criterion. The surfaces in the 3D view are coloured using C_P contours and the streamtraces are coloured with X vorticity.

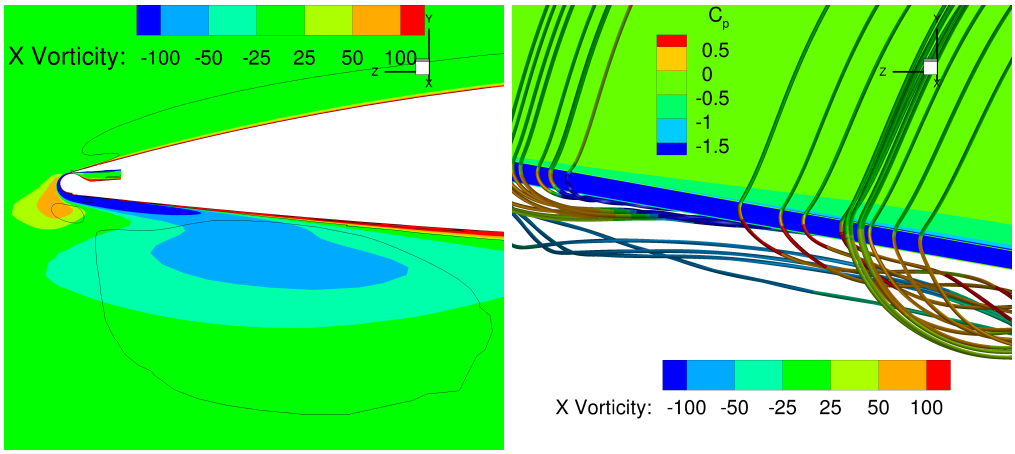

(a) Slice at x=0.962 (b) 3D view near the center of the wing

Figure 16: Slice and 3D view near the center of the SACCON's right wing. The slice has been coloured using X-vorticity contours and the regions enclosed by black lines are regions identified as vortices by the λ_2 criterion. The surfaces in the 3D view are coloured using C_P contours and the streamtraces are coloured with X vorticity.

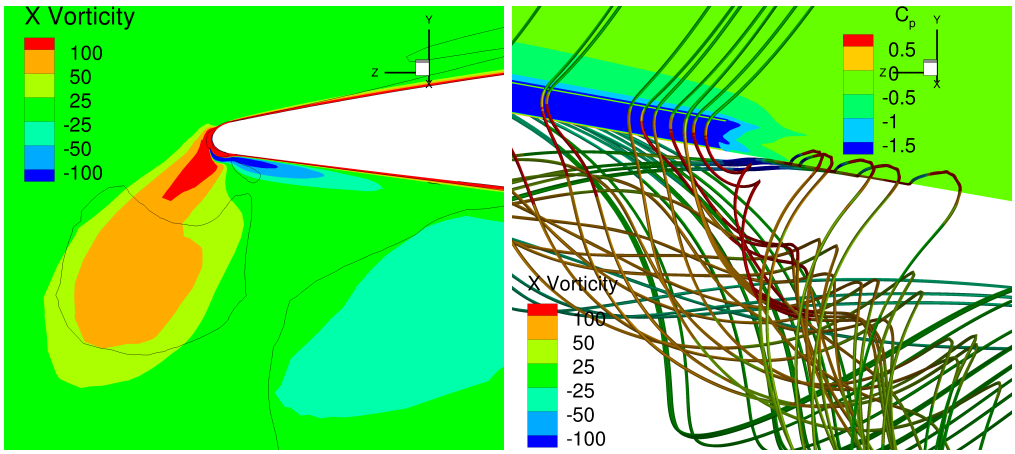

(a) Slice at x=1.151 (b) 3D view.

Figure 17: Slice and 3D view near the tip of the SACCON's right wing. The slice has been coloured using X-vorticity contours and the regions enclosed by black lines are regions identified as vortices by the λ_2 criterion. The surfaces in the 3D view are coloured using C_P contours and the streamtraces are coloured with X vorticity.

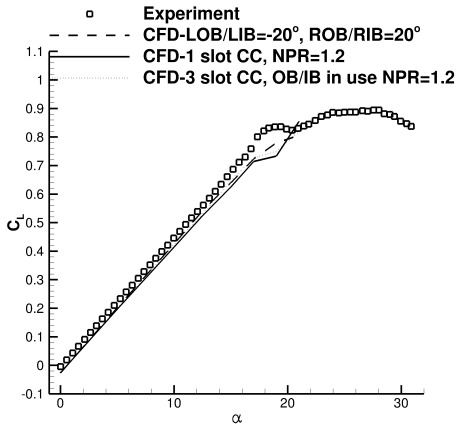

(a) Lift Coefficient

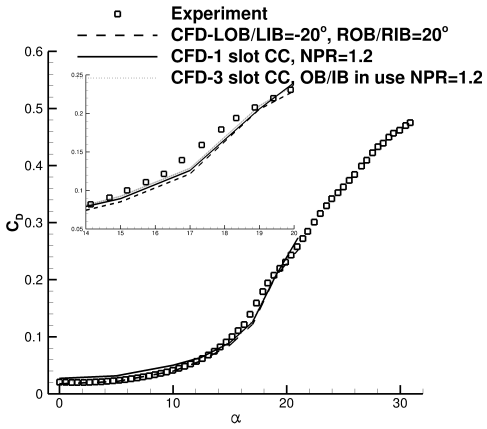

(b) Drag Coefficient

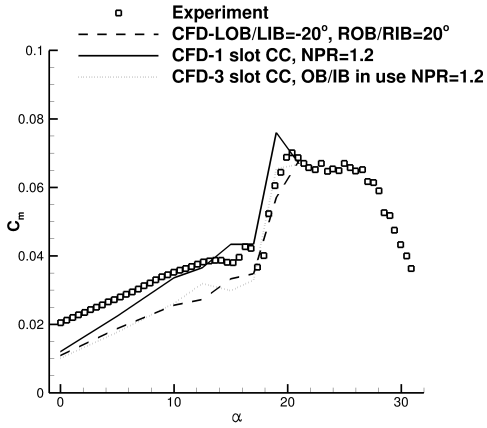

(c) Pitching Moment Coefficient

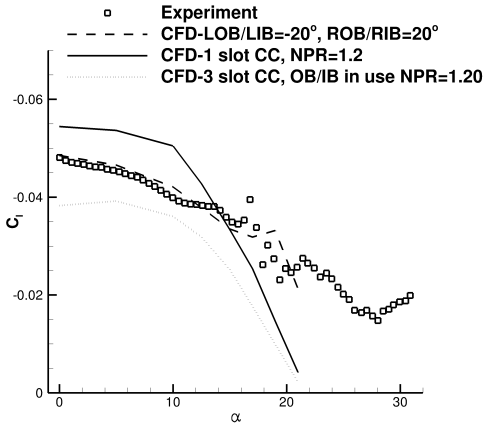

(d) Rolling Moment Coefficient

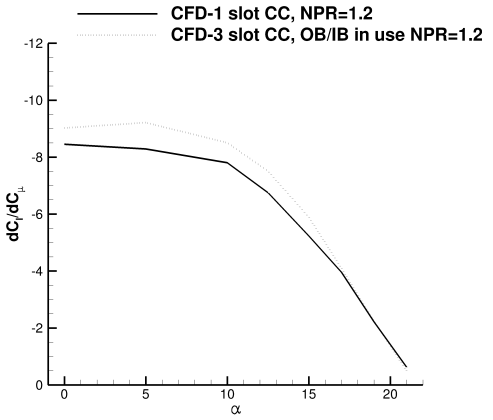

(e) Roll Moment Coefficient/Momentum Coefficient

Figure 18: Comparison of the loads from the experiments with LOB/LIB at $-20°$ and ROB/RIB at $20°$, the integrated loads from the CFD results with the same flap settings and the integrated loads from the CFD result of the SACCON with trailing edge CC at a NPR of 1.20.

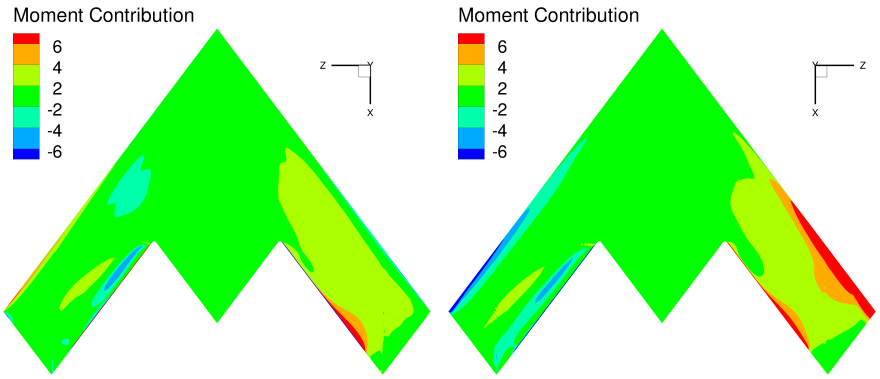

(a) AoA=0°, upper surface

(b) AoA=0°, lower surface

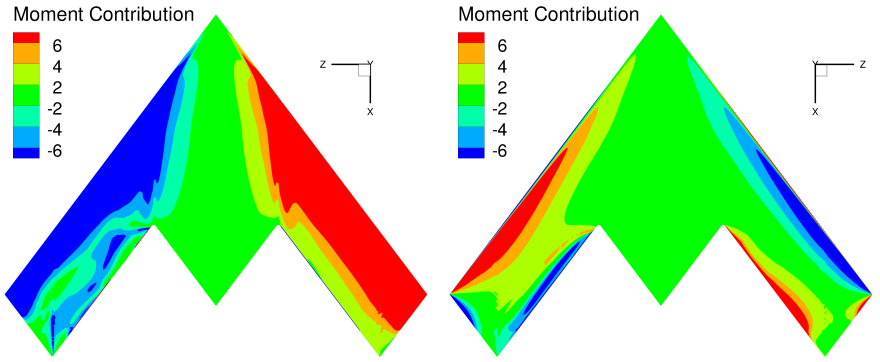

(c) AoA=15°, upper surface

(d) AoA=15°, lower surface

Figure 19: Plot showing the contribution to the roll moment for 0° and 15° for the SACCON with the single slot CC.

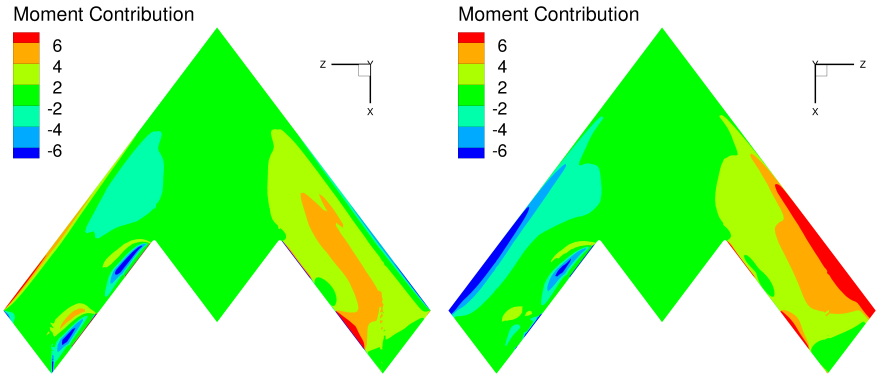

(a) AoA=0°, upper surface

(b) AoA=0°, lower surface

Figure 20: Plot showing the contribution to the roll moment for 0° and 15° for the SACCON with the three slot CC.

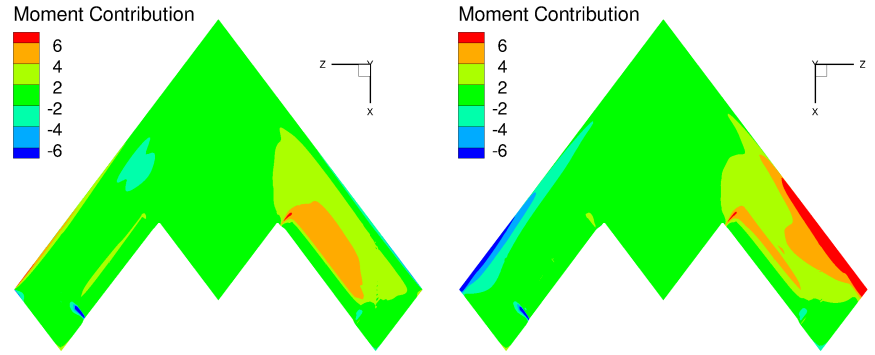

(a) AoA=0°, upper surface

(b) AoA=0°, lower surface

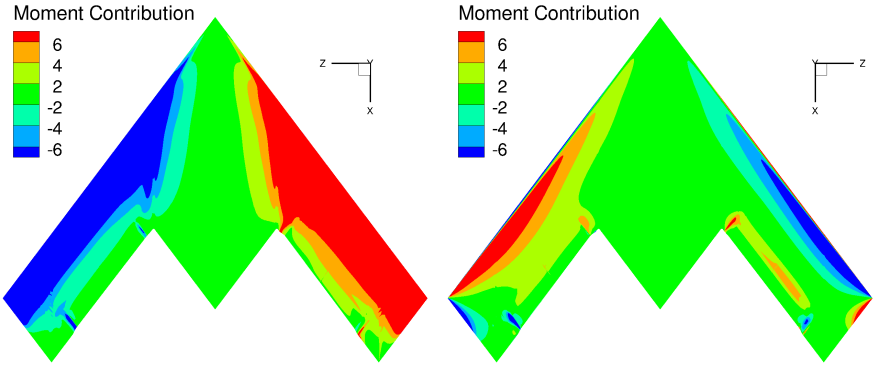

(c) AoA=15°, upper surface

(d) AoA=15°, lower surface

Figure 21: Plot showing the contribution to the roll moment for 0° and 15° for the SACCON with conventional control surfaces.

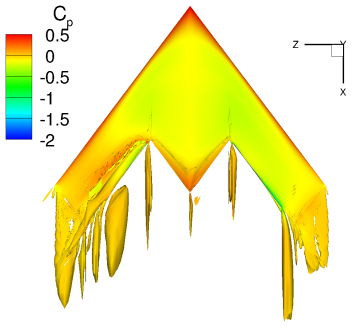

(a) Single slot, AoA=0°, upper surface

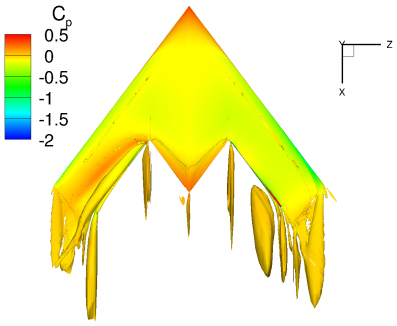

(b) Single slot, AoA=0°, lower surface

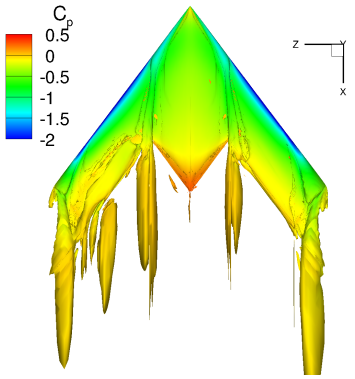

(c) Single slot, AoA=15°, upper surface

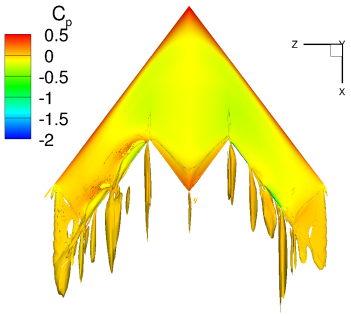

(d) Three slot, AoA=0°, upper surface

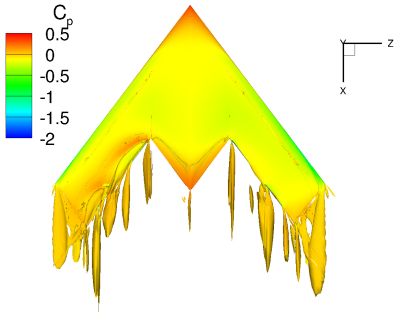

(e) Three slot, AoA=0°, lower surface

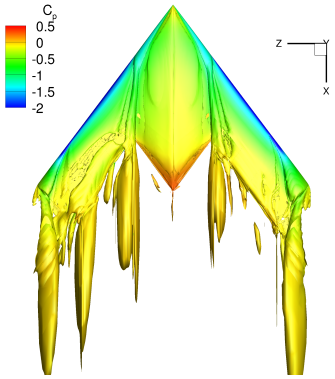

(f) Three slot, AoA=15°, upper surface

Figure 22: Iso-surfaces of the λ_2 criterion coloured with C_p for the SACCON employing circulation control at 0° and 15°.